frontiers | Frontiers in Mechanical Engineering

ORIGINAL RESEARCH
published: 05 August 2022
doi: 10.3389/fmech.2022.957859

Assessing the Lightweight Potential of Additively Manufactured Metals by Density-Specific Woehler and Shiozawa Diagrams

Mohamed Merghany, Mirko Teschke, Felix Stern, Jochen Tenkamp and Frank Walther*

Chair of Materials Test Engineering (WPT), TU Dortmund University, Dortmund, Germany

Additive manufacturing (AM) using the powder bed fusion (PBF) process is building up the components layer by layer, which enables the fabrication of complex 3D structures with unprecedented degrees of freedom. Due to the high cooling rates of the AM process, fine microstructures are generated. This leads to an improvement in quasistatic properties such as tensile strength, whereas the fatigue strength is comparable to that of conventionally manufactured metal or even reduced. This is due to the presence of process-induced defects formulated during the manufacturing process in combination with the increased notch stress sensitivity of high-strength metals. In this work, the fatigue damage assessment using different approaches like those of Murakami and Shiozawa for three AM alloys (AlSi10Mg, 316L, and TNM-B1) containing defects is studied for better understanding of capability and mechanisms. Moreover, the effect of the lightweight potential is investigated, and how the specific material density can be considered when the fatigue damage tolerance is characterized.

Keywords: laser powder bed fusion (PBF-LB), electron beam powder bed fusion (PBF-EB), AlSi10Mg, 316L, TiAl, fatigue behavior, fatigue damage tolerance

OPEN ACCESS

Edited by:
Gang Jl,
National Centre for Scientific Research, France

Reviewed by:
Yong Luo,
China University of Mining and Technology, China
Mário S. Correia,
Polytechnic Institute of Leiria, Portugal

****Correspondence:***
Mohamed Merghany
mohamed.merghany@tu-dortmund.de

Specialty section:
This article was submitted to Digital Manufacturing, a section of the journal Frontiers in Mechanical Engineering

Received: *31 May 2022*
Accepted: *24 June 2022*
Published: *05 August 2022*

Citation:
Merghany M, Teschke M, Stern F, Tenkamp J and Walther F (2022) Assessing the Lightweight Potential of Additively Manufactured Metals by Density-Specific Woehler and Shiozawa Diagrams. Front. Mech. Eng 8:957859. doi: 10.3389/fmech.2022.957859

1 INTRODUCTION

The AM process can produce complex near net shape parts, for example, with internal cooling or heating channels, bionic structures, or dental implants that conventional manufacturing processes cannot (Bose et al., 2013; Wang et al., 2016). AM processes have been rapidly advancing into various industries, such as aerospace, automotive, medical, architecture, and construction. They are now not only used in the visualization and prototyping stages but also transferred into functional and actual part replacement, which opens further design possibilities and challenges (Al Rashid et al., 2020). Laser powder bed fusion of metals (PBF-LB) and electron beam powder bed fusion (PBF-EB) are competitive processes due to their ability to produce complex and precious parts. While PBF-LB shows better surface roughness and lower production costs than PBF-EB (Merkt et al., 2015), the high process temperatures and vacuum atmosphere prevent cracking and oxidation in PBF-EB (Körner, 2016). Although AM enables the fabrication of complex 3D structures with unprecedented degrees of freedom, this can lead to structures and design issues inconclusively answered with respect to part density, defect distribution, and fatigue behavior (Aboulkhair et al., 2019). In addition to the defect size, defect shape, and defect distribution, the distance between the defects and the surface also plays a crucial role with regard to fatigue behavior. Therefore, the comparison between different processes with different process-induced defect distributions is difficult.

Fatigue mechanisms and their prediction are still challenging due to different factors that impact fatigue performance significantly. Materials containing defects are limited in their fatigue lifetimes due to frequently occurring crack initiation and propagation. Therefore, different approaches for materials containing defects have been proposed. The empirical approach of Murakami describes defects as pre-existing (short) cracks having a crack threshold proportional to the fatigue limit. The square root of the surface area of the defect in the plane perpendicular to the maximum principal stress direction is defined as the equivalent failure-initiating defect size parameter (a_i) (Murakami, 2012). The cyclic stress intensity factor range (ΔK_i) can be calculated based on the defect size as per the following **Eq. 1** (Noguchi et al., 2007).

$$\Delta K_i = Y \cdot \Delta\sigma \cdot \sqrt{\pi \cdot a_i} \quad \begin{matrix}\text{Surface: Y = 0.65} \\ \text{Volume: Y = 0.50}\end{matrix} \tag{1}$$

$$a_i = \sqrt{A_i} \tag{2}$$

where (Y) is the shape factor, (a_i) is the failure-initiating defect size (**Eq. 2**), ($\Delta\sigma$) is the applied stress range, and (A_i or $area_i$) is the projected cross-sectional area of the failure-initiating defect perpendicular to the loading direction equal to the equivalent defect size (a_i).

Moreover, the model introduced by Shiozawa et al. (Shiozawa and Lu, 2008) for crack propagation–dominant parts can be used for a better representation and interpretation of the fatigue results. Here, as shown in **Eq. 3**, using various assumptions, the Paris–Erdogan law for describing the crack propagation behavior is integrated from the initial defect size to the critical crack size.

$$\Delta K_i = \left[\frac{C(m-2)}{2}\right]^{-1/m} \cdot \left(\frac{N_f}{a_i}\right)^{-1/m} \tag{3}$$

where (C) and (m) are assumptions for Paris law coefficients and (N_f) is the number of cycles to failure. (N_f/a_i) is the so-called defect-related fatigue lifetime.

Lightweight potential describes the potential of a substitution of a certain shape, material, or technology for a respective counterpart. When considering a substitution of a certain material for another lightweight new material to withstand the same stresses and to carry out the same function, for instance, this material has a high lightweight potential compared to the old one (Al Rashid et al., 2020). Due to this within this work, the lightweight potential should be assessed by specific Woehler and Shiozawa diagrams, and the differences and advantages are discussed.

2 MATERIALS AND METHODS

2.1 Materials

Three additively manufactured alloys are investigated: the aluminum alloy AlSi10Mg, the stainless steel AISI 316L (X2CrNiMo18-15-3), and the titanium aluminide alloy TNM-B1 (Ti-46.5Al-4Nb-1Mo-0.1B) for their differences in specific densities from the lowest density of AlSi10Mg to the highest density of 316L.

AlSi10Mg and 316L stainless steel specimens were produced with PBF-LB using an EOS M290 system. Further information about the manufacturing process of AlSi10Mg can be found in the study by Tenkamp et al., (2022). Additionally, two types of test specimens with different intended pre-defined defect sizes in form of cuboid cavities with an edge length of 1.0 and 1.5 mm are produced for 316L. Detailed information about the manufacturing process can be found in the study by Kotzem et al., (2021). Finally, TNM-B1 specimens were manufactured by PBF-EB on an Arcam A2X system. In addition to the as-built condition, half of the specimens were hot isostatically pressed. This allowed the investigation of two microstructurally comparable states with a variation in defect type and size. Detailed information about the manufacturing process can be found in the studies by Moritz et al., (2021); Teschke et al., (2022). AlSi10Mg specimens were manufactured vertically, parallel to the building direction. 316L and TNM specimens were manufactured horizontally, perpendicular to the building direction.

AlSi10Mg, 316L, and half of TNM-B1 specimens were investigated in the as-built (AB) condition without post-process heat treatment, while half of the TNM-B1 specimens were hot isostatically pressed (HIP). All specimens were tested at room temperature (RT). More detailed information about the micro-structure and tensile testing results can be found in the studies by Kotzem et al., (2021); Tenkamp et al., (2022); Teschke et al., (2022).

2.2 Methods

2.2.1 Fatigue Testing

For the AlSi10Mg alloy, stress-controlled fatigue tests were performed using a Rumul Testronic 150 kN resonant fatigue testing system with a 20 kN load cell at a test frequency of f = 70 Hz and fully reversed loading with a stress ratio of R = −1 up to 10^7 cycles. For 316L steel, stress-controlled fatigue tests were carried out on the servo-hydraulic testing system Schenck PSB100 with an Instron 8800 controller (100 kN load cell) at a test frequency of f = 20 Hz and a stress ratio of R = −1 up to 10^7 cycles. For the TNM-B1 alloy, the fatigue tests were performed stress-controlled on the servo-hydraulic testing system Instron 8801 (100 kN load cell) at a test frequency of f = 20 Hz and a stress ratio of R = −1 up to $2{\cdot}10^6$ cycles. The test frequencies were selected to be material-specific to minimize self-heating of specimens during fatigue testing to a maximum of 15 K. Hereby, no significant frequency effect is assumed between 20 and 70 Hz testing. All specimens are grinded and polished up to 1 µm diamond suspension. A surface roughness of $R_Z \leq 0.8$ µm has to be reached to minimize surface effects.

2.2.2 Macro-Hardness Measurement

The hardness of the three alloys was determined by Vickers macro-hardness HV10 measurements using the Wolpert Dia-

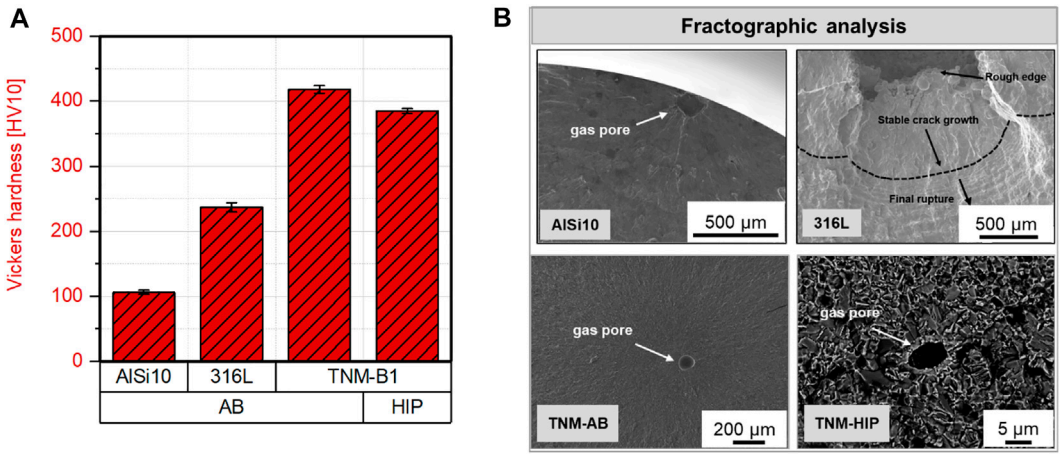

FIGURE 1 | (A) Vickers hardness. **(B)** Fractographic analyses for AlSi10Mg (Tenkamp et al., 2022), 316L (Kotzem et al., 2021), and TNM-B1 (Teschke et al., 2022)

Testor 2Rc testing system. For each alloy, the hardness measurements were performed according to DIN EN ISO 6507-1, and then the mean value and standard deviation were calculated.

2.2.3 Fractographic Analysis

The microstructure and fracture surfaces of all specimens were examined using a scanning electron microscope (SEM) Tescan MIRA3 XMU to determine the location, size, and shape of the failure-initiating defect. These parameters were determined by post-processing of the obtained SEM images using ImageJ software. The porosity and defect distributions were characterized using microfocus-computed tomography (µ-CT) Nikon XT H160, where the parts' relative densities and the equivalent defect size a_i were also quantified.

3 RESULTS AND DISCUSSION

3.1 Hardness and Fractography Analysis Results

The results of Vickers hardness measurements for the three alloys are shown in **Figure 1A**. It is observed that TNM-B1 showed the highest hardness compared to the other alloys, which have a hardness value of 418 ± 6 HV10 for the AB condition and 385 ± 4 HV10 for the HIP condition. This includes the fact that HIP led to a decrease in hardness. AlSi10Mg has the lowest hardness value, 106 ± 3 HV10, while 316L has an intermediate hardness value equal to 237 ± 7 HV10.

Based on SEM and µCT results, the intended defect size of 316L has the largest value of either 958 or 1,463 µm with only slight deviations (Kotzem et al., 2021) and the lowest value for TNM-B1 with an average of 64 ± 25 µm for the AB condition and 20 ± 8 µm for the HIP condition, which means that the HIP process was able to decrease the equivalent defect size. AlSi10Mg has an average defect size equal to 242 ± 133 µm. Some of the fractographic analyses using SEM for different defects for three alloys are shown in **Figure 1B**.

3.2 Fatigue Testing Results

After fatigue testing of the three alloys at different stress amplitudes with a stress ratio R = −1, a combined Woehler diagram for the three alloys is constructed by plotting the stress amplitude σ_a vs. the number of cycles to failure N_f in log-log scale. It is obtained from the Woehler diagram in **Figure 2A** that AlSi10Mg has the lowest fatigue strength due to the low hardness and large defect size. The verifying defect size was responsible for increasing the scattering within the Woehler diagram. TNM-B1 has the highest fatigue strength and lifetime compared to 316L and AlSi10Mg, and this correlates with its higher hardness and smaller defect size. Moreover, the HIP condition has improved the fatigue strength and damage tolerance by reducing the number and size of the defects, and the fatigue strength ($2{\cdot}10^6$ cycles) could be further increased by 42%–500 MPa.

Figure 2B shows the specific Woehler diagram for the three alloys by dividing the stress amplitude by the alloy density. Density of AlSi10Mg is equal to ≈2,650 kg/m^3 ([1]), that of 316L is equal to ≈8,000 kg/m^3 ([2]), and that of TNM-B1 is equal to ≈4,160 kg/m^3 (Loeber et al., 2014). It clearly shows the high fatigue strength and lightweight potential of TNM-B1 compared to 316L and AlSi10Mg alloys. While 316L and AlSi10Mg have comparable specific low cycle fatigue (LCF) strength, the lightweight potential in the HCF regime is significantly increased for 316L compared to AlSi10Mg (+43%). It is concluded that TNM-B1 has the highest lightweight potential compared to that of the others, leading to a factor 3-5.

The Shiozawa diagram considers the failure-initiating defect size, and it can describe the damage tolerance more efficiently for the alloys. The Shiozawa diagram is corrected for the defect size; therefore, it was able to decrease the scattering in the Woehler diagram that was generated from the different defect sizes. This can be observed where the coefficient of determination improved for AlSi10Mg from R^2 = 0.66 in the

[1]N.N.: SLM Solutions: Material data sheet, Al-Alloy AlSi10Mg.
[2]N.N.: SLM Solutions: Material data sheet, Fe-Alloy 316L.

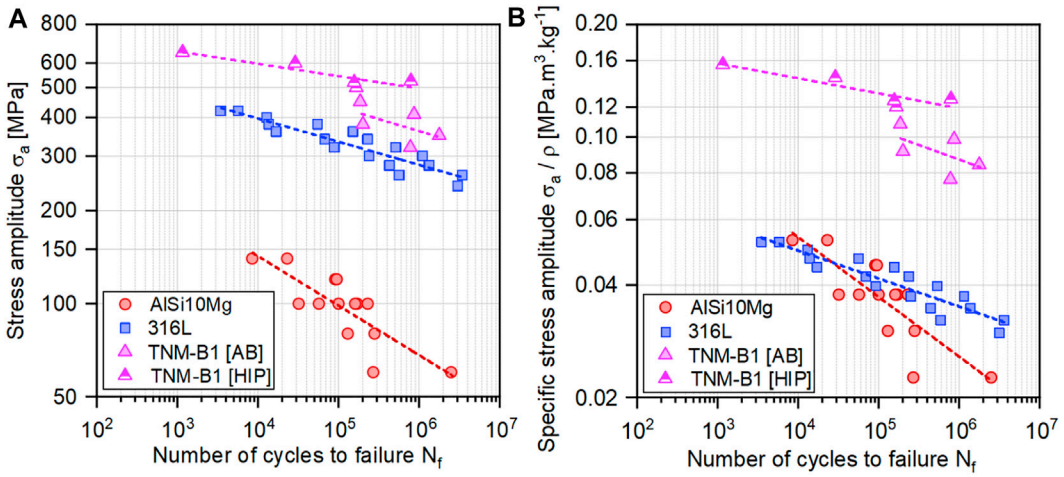

FIGURE 2 | (A) Woehler diagrams; **(B)** specific Woehler diagrams for AlSi10Mg, 316L (Kotzem et al., 2021; Stern et al., 2022), and TNM-B1 (Teschke et al., 2022) alloys.

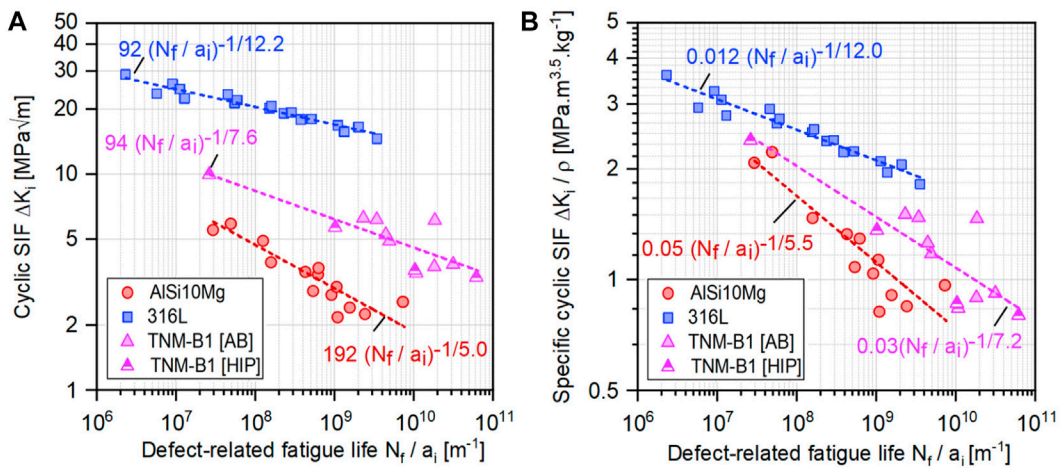

FIGURE 3 | (A) Shiozawa diagrams. **(B)** Specific Shiozawa diagrams for AlSi10Mg (Tenkamp et al., 2022), 316L (Kotzem et al., 2021; Stern et al., 2022), and TNM-B1 (Teschke et al., 2022) alloys.

Woehler curve to $R^2 = 0.81$ in the Shiozawa curve. R^2 improved to 0.94 and 0.72 for 316L and TNM-B1, respectively. **Figure 3A** shows the combined Shiozawa diagram for the three alloys. The cyclic stress intensity factor (SIF) ΔK_i is plotted vs. the defect-related fatigue life N_f/a_i. It is obtained that 316L has the highest fatigue defect tolerance (FDT) compared to that of AlSi10Mg and TNM-B1. AlSi10Mg has the significantly lowest FDT. For all alloys, there is no significant difference of FDT in the LCF and HCF regimes. **Figure 3B** shows the specific Shiozawa diagram for the alloys by dividing ΔK_i by the alloy density and plotting versus N_f/a_i. It is observed that 316L has the highest specific FDT, while AlSi10Mg has the lowest. In summary, the FDT and specific FDT correlate with the elastic modulus of each alloy. Therefore, it could be assumed that the intrinsic crack growth threshold is responsible for the (specific) FDT as it only depends on the elastic modulus of the alloy and not on further mechanical or structural properties. (Wasén and Heier, 1998; Maierhofer et al., 2018).

4 CONCLUSION AND OUTLOOK

It was found that the defects in AM alloys have a high effect on the fatigue lifetime. It is also obtained from the specific Woehler curve that the lightweight potential for TNM-B1 has the highest value, followed by 316L and AlSi10Mg. Comparing Woehler and Shiozawa curves, it is concluded that the defect size (a_i) introduced by Murakami is particularly suitable for the geometric description of the

defect as an initial defect or crack size, while the model presented by Shiozawa takes this influence into account and enables a "defect-based" representation of the fatigue behavior. Therefore, the Shiozawa diagram improves the fatigue assessment of defective materials as it enables a fatigue defect or damage tolerant assessment. The specific Shiozawa curves show that the 316L really has the highest lightweight potential by taking the alloy-specific stress amplitudes, density, and defects into account. Therefore, for releasing the full lightweight potential, a stress- and defect-based assessment is necessary and can be reached by using density-specific Shiozawa diagrams.

In future investigations, the effect of the intrinsic crack growth threshold should be included to further understand the structural and mechanical reasons for the specific fatigue damage tolerance of steel, Ti, and Al alloys.

DATA AVAILABILITY STATEMENT

The raw data supporting the conclusions of this article will be made available by the authors, without undue reservation.

AUTHOR CONTRIBUTIONS

MM: writing, concept, and results of Al material. MT: writing and results of Ti-Al material. FS: writing and results of 316L material. JT: writing, concept, funding, and results of Al material. FW: writing, concept, review, and funding.

FUNDING

The authors thank the German Research Foundation (Deutsche Forschungsgemeinschaft, DFG) for its financial support within the research projects "Mechanism-based investigation of additively-manufactured aluminum matrix composites (AMC) for enhanced mechanical strength" (project no. 425479688), "Mechanism-based assessment of the influence of powder production and process parameters on the microstructure and the deformation behavior of SLM-compacted C+N steels in air and in corrosive environments" (project no. 372290567), and "Microstructure and defect-controlled additive manufacturing of gamma titanium aluminides for function-based control of local materials properties" (project no. 404665753).

REFERENCES

Aboulkhair, N. T., Simonelli, M., Parry, L., Ashcroft, I., Tuck, C., and Hague, R. (2019). 3D Printing of Aluminium Alloys: Additive Manufacturing of Aluminium Alloys Using Selective Laser Melting. *Prog. Mater. Sci.* 106, 100578. doi:10.1016/j.pmatsci.2019.100578

Al Rashid, A., Khan, S. A., G. Al-Ghamdi, S., and Koç, M. (2020). Additive Manufacturing: Technology, Applications, Markets, and Opportunities for the Built Environment. *Automation Constr.* 118, 103268. doi:10.1016/j.autcon.2020.103268

Bose, S., Vahabzadeh, S., and Bandyopadhyay, A. (2013). Bone Tissue Engineering Using 3D Printing. *Mater. Today* 16 (12), 496–504. doi:10.1016/j.mattod.2013.11.017

Körner, C. (2016). Additive Manufacturing of Metallic Components by Selective Electron Beam Melting — a Review. *Int. Mater. Rev.* 61, 361–377. doi:10.1080/09506608.2016.1176289

Kotzem, D., Kleszczynski, S., Stern, F., Elspaß, A., Tenkamp, J., Witt, G., et al. (2021). Impact of Single Structural Voids on Fatigue Properties of AISI 316L Manufactured by Laser Powder Bed Fusion. *Int. J. Fatigue* 148, 106207. doi:10.1016/j.ijfatigue.2021.106207

Loeber, L., Schimansky, F. P., Kuehn, U., Pyczak, F., and Eckert, J. (2014). Selective Laser Melting of a Beta-Solidifying TNM-B1 Titanium. *J. Mater. Process. Technol.* 214, 1852–1860.

Maierhofer, J., Kolitsch, S., Pippan, R., Gänser, H.-P., Madia, M., and Zerbst, U. (2018). The Cyclic R-Curve – Determination, Problems, Limitations and Application. *Eng. Fract. Mech.* 198, 45–64. doi:10.1016/j.engfracmech.2017.09.032

Merkt, S., Hinke, C., Bültmann, J., Brandt, M., and Xie, Y. M. (2015). Mechanical Response of TiAl6V4 Lattice Structures Manufactured by Selective Laser Melting in Quasistatic and Dynamic Compression Tests. *J. Laser Appl.* 27, 1–7. doi:10.2351/1.4898835

Moritz, J., Teschke, M., Marquardt, A., Stepien, L., López, E., Brückner, F., et al. (2021). Electron Beam Powder Bed Fusion of γ-titanium Aluminide: Effect of Processing Parameters on Part Density, Surface Characteristics, and Aluminum Content. *Metals* 11, 1093. doi:10.3390/met11071093

Murakami, Y. (2012). Material Defects as the Basis of Fatigue Design. *Int. J. Fatigue* 41, 2–10. doi:10.1016/j.ijfatigue.2011.12.001

Noguchi, H., Morishige, K., Fujii, T., Kawazoe, T., and Hamada, S. (2007). Proposal of method for estimation stress intensity factor range on small crack for light metals. Proceedings of the 56th JSMS Annual Meetings, Japan, May, 2007, 137–138.

Shiozawa, K., and Lu, L. (2008). Effect of Non-metallic Inclusion Size and Residual Stresses on Gigacycle Fatigue Properties in High Strength Steel. *Adv. Mater. Res.* 44-46, 33–42. doi:10.4028/www.scientific.net/amr.44-46.33

Stern, F., Grabowski, J., Elspaß, A., Kotzem, D., Kleszczynski, S., Witt, G., et al. (2022). Influence Assessment of Artificial Defects on the Fatigue Behavior of Additively Manufactured Stainless Steel 316LVM. *Procedia Struct. Integr.* 37, 153–158. doi:10.1016/j.prostr.2022.01.071

Tenkamp, J., Stern, F., and Walther, F. (2022). Uniform Fatigue Damage Tolerance Assessment for Additively Manufactured and Cast Al-Si Alloys: An Elastic-Plastic Fracture Mechanical Approach. *Addit. Manuf. Lett.* 3, 100054. doi:10.1016/j.addlet.2022.100054

Teschke, M., Moritz, J., Tenkamp, J., Marquardt, A., Leyens, C., and Walther, F. (2022).Defect-based Characterization of the Fatigue Behavior of Additively Manufactured Titanium Aluminides, *Int. J. Fatigue*, 163. arXiv, 107047. doi:10.1016/j.ijfatigue.2022.107047

Wang, X., Xu, S., Zhou, S., Xu, W., Leary, M., Choong, P., et al. (2016). Topological Design and Additive Manufacturing of Porous Metals for Bone Scaffolds and Orthopaedic Implants: A Review. *Biomaterials* 83, 127–141. doi:10.1016/j.biomaterials.2016.01.012

Wasén, J., and Heier, E. (1998). Fatigue Crack Growth Thresholds—The Influence of Young's Modulus and Fracture Surface Roughness. *Int. J. Fatigue* 20, 737–742. doi:10.1016/s0142-1123(98)00034-6

Conflict of Interest: The authors declare that the research was conducted in the absence of any commercial or financial relationships that could be construed as a potential conflict of interest.

Publisher's Note: All claims expressed in this article are solely those of the authors and do not necessarily represent those of their affiliated organizations, or those of the publisher, the editors, and the reviewers. Any product that may be evaluated in this article, or claim that may be made by its manufacturer, is not guaranteed or endorsed by the publisher.